Exchange bias effect in hybrid improper ferroelectricity $Ca_{2.94}Na_{0.06}Mn_2O_7$

Songyang Li, Shouyu Wang, Yangong Lu, Chuang Zhang, Xiaoxia Yang, Ju Gao, Dejun Li, Yun Zhu, and Weifang Liu

Citation: AIP Advances **8**, 015009 (2018); doi: 10.1063/1.5003877
View online: https://doi.org/10.1063/1.5003877
View Table of Contents: http://aip.scitation.org/toc/adv/8/1
Published by the American Institute of Physics

Exchange bias effect in hybrid improper ferroelectricity $Ca_{2.94}Na_{0.06}Mn_2O_7$

Songyang Li,[1] Shouyu Wang,[1,a] Yangong Lu,[1] Chuang Zhang,[1]
Xiaoxia Yang,[1] Ju Gao,[2] Dejun Li,[1] Yun Zhu,[1] and Weifang Liu[3,b]
[1]*College of Physics and Materials Science, Tianjin Normal University, Tianjin 300387, China*
[2]*Department of Physics, University of Hong Kong, Pokfulam Road, Hong Kong, China*
[3]*Tianjin Key Laboratory of Low-Dimensional Materials, Physics and Preparing Technology, Faculty of Science, Tianjin University, Tianjin 300072, China*

(Received 8 September 2017; accepted 21 December 2017; published online 9 January 2018)

The hybrid improper ferroelectricity $Ca_3Mn_2O_7$ (CMO) has been a subject of remarkable interest due to potential multiferroicity. In this paper we synthesized CMO and $Ca_{2.94}Na_{0.06}Mn_2O_7$ (CNMO) ceramics and investigated their structural and magnetic properties. It is found that Na doping effectively weakens the structural distortion as decreasing the orthorhombic distortion and Jahn-Teller distortion. Although both samples undergo an antiferromagnetic transition at temperature around 111 K, the exchange bias and coercive fields increase in CNMO. Such increased exchange bias field could be explained within a model of size-variable nanoscale ferromagnetic clusters embedded in an antiferromagnetic matrix.
https://doi.org/10.1063/1.5003877

INTRODUCTION

In recent years, the hybrid improper ferroelectricity (HIF) has attracted considerable attention due to its great potential technological application in creating room temperature multiferroicity with strong magnetoelectric coupling induced by the same lattice instability. The HIF, characterized as the improper ferroelectricity, is a mechanism where the spontaneous polarization results from the hybridization of two or more of non-ferroelectric structural order parameters, and was predicted for a number of compounds including double-layered orthorhombic $Ca_3Ti_2O_7$, $Ca_3Mn_2O_7$ and $(Ca/Sr/Ba)_3(Sn/Zr/Ge)_2O_7$.[1–3] Especially, $Ca_3Mn_2O_7$ has been a subject of remarkable interest and been widely investigated in last several years, since the theoretical first-principles calculations demonstrate that MnO_6 octahedrons distortions simultaneously induce ferroelectricity, magnetoelectricity and weak ferromagnetism.[1,4]

$Ca_3Mn_2O_7$, as a geometric ferroelectricity, is a member of Ruddlesden-Popper systems: $A_{n+1}B_nC_{3n+1}$ (i.e. with A = Ca ion, B = Mn ion, C = O ion and $n = 2$, respectively), where two-layer $CaMnO_3$ perovskite blocks of corner-sharing MnO_6 octahedrons with neighboring blocks separated along the perovskite a axis by an extra CaO rock-salt layer, as shown in Fig. 1(b). And its crystal structure is orthorhombic with space group $Cmc2_1$ at room temperature.[5] Zhu et al. and Lobanov et al. found that $Ca_3Mn_2O_7$ undergoes a G-type antiferromagnetic (AFM) transition with Néel temperature (T_N) ≈ 115 K.[6,7] Benedek and Fennie have proposed a route to realize magnetoelectric coupling with MnO_6 octahedrons rotation and tilt distortions in multiferroics.[1] It is a known fact that cation substitution can provide an effective tool for tailoring the crystal structure and physicochemical properties of metal oxides. Lobanov et al. found that doping in $Ca_3Mn_2O_7$ with tetravalent Th at the Ca-site leads to the development of long-range ordered ferromagnetic (FM) phase in AFM matrix.[8]

[a]E-mail address: sywang@mail.tjnu.edu.cn
[b]E-mail address: wfliu@tju.edu.cn

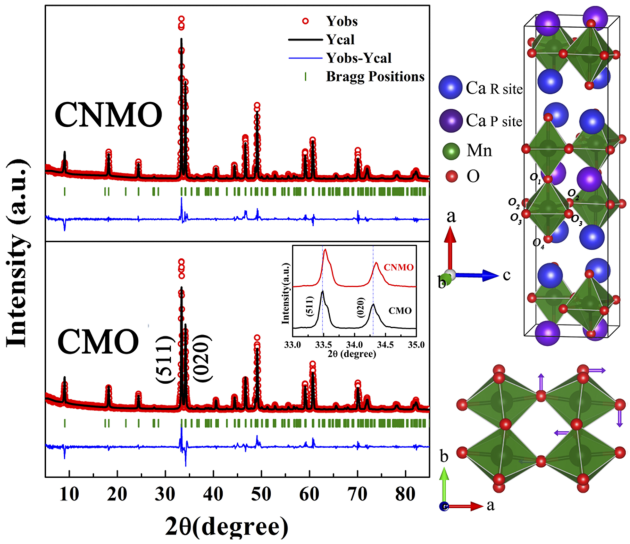

FIG. 1. (a) Rietveld-refined XRD patterns of CMO and CNMO ceramics at room temperature. Inset is the enlarged views of the diffraction peaks located at about $2\theta = 34°$ (b) and (c) The unit cell structure of CMO at normal conditions could be considered as distorted perovskite with strongly distorted MnO_6 octahedrons.

Toyoda et al. reported that low content of La doping at the Ca-site in $Ca_3Mn_2O_7$ leads to the appearance of thermoelectric properties at high temperature.[9]

In fact, it has been reported that substitution of the monovalent cation Na can effectively improve the physicochemical properties in other $A_{n+1}B_nC_{3n+1}$ types of perovskite materials, such as the development of negative magnetic susceptibility below 40 K in $(Ca_{1-x}Na_x)_2MnO_4$ ceramics ($n = 1$)[10] and the existence of exchange bias (*EB*) effect in $Bi_{1-x}Na_xFeO_3$ nanoparticles ($n = \infty$).[11] The *EB* effect is a widespread phenomenon in ABO_3 perovskite compounds (e.g. $CaMnO_3$, $LaMnO_3$ and $BiFeO_3$), but up till now there is no report about the *EB* effect in $Ca_3Mn_2O_7$ series. In this study, we synthesized $Ca_3Mn_2O_7$ (CMO) and $Ca_{2.94}Na_{0.06}Mn_2O_7$ (CNMO) ceramics and studied their structural and magnetic properties. It is found that Na doping effectively weakens the structural distortion and increases the *EB* field.

EXPERIMENT

The CMO and CNMO samples were prepared by the standard solid-state reaction method. Stoichiometric mixtures of high purity (99.99%) oxides $CaCO_3$, MnO_2 and Na_2CO_3 were milled for 6 h in agate mortars with alcohol. After drying, these homogeneous mixtures were first calcined at 1000 °C for 12 h in air. The powder obtained were milled for another 6 h, hydrostatically cold pressed into 1 mm thick disks and sintered at 1300 °C for 72 h in air.

The crystalline structure analysis of the samples was carried out by X-ray diffraction (XRD) (Rigaku D/MAX-2500 diffractometer with Cu-K_α radiation). Raman spectra were recorded with the LabRAM XploRA PLUS detector (made by HORIBA Jobin Yvon, France). The chemical states of Mn ions were analyzed by X-ray photoelectron spectroscopy (XPS), which was recorded with PHI1600 ESCA System (Perkin Elmer, USA). Morphological study of both samples were investigated using scanning electron microscopy (SEM) (made by Hitachi Co., Tokyo, Japan). All above measurements were carried out at room temperature. Magnetic characterization of the samples was measured on the Magnetic Property Measurement System (MPMS) SQUID-VSM (Quantum Design) at various temperature.

RESULTS AND DISCUSSION

Fig. 1(a) displays the Rietveld refined XRD patterns of CMO and CNMO samples. All the main XRD diffraction peaks can be well fitted with the orthorhombic perovskite Runddlesden-Popper

TABLE I. Structure parameters obtained from Rietveld refinement of CMO and CNMO samples.

Modes	a (Å)	b (Å)	c (Å)	V (Å^3)	$\delta\times10^4$	*R*-factors (%)		
						R_p	R_{wp}	χ^2
CMO	19.4403	5.2447	5.2353	533.78	8.93	14.6	16.3	2.9
CNMO	19.4280	5.2410	5.2338	532.92	6.89	13.8	16.3	3.0

structure (space group $Cmc2_1$). Structural parameters obtained from the Rietveld refined XRD patterns for both samples are shown in Table I and Table II. It can be clearly observed that the cell volume decreases from 533.78 Å^3 for CMO to 532.92 Å^3 for CNMO. The enlarged view of the two strongest diffraction peaks located at about $2\theta = 34°$ is shown in the inset of Fig. 1(a). It can be seen that diffraction peaks in CNMO show an observable shift toward a high degree. The ionic radius of Na^+ (1.16 Å) is slightly larger than that of Ca^{2+} (1.14 Å),[12] which doesn't account for the decrease in the cell volume. We ascribe the lattice contraction in CNMO to the transformation of partial Mn^{3+} (0.64 Å) ions to Mn^{4+} (0.53 Å)[12] induced by the substitution of Ca^{2+} by Na^+, so as to keep the charge balance in nature. This transformation has been confirmed by the X-ray photoelectron spectroscopic (XPS) measurement result, as shown in Fig. 4, that the ratio of Mn^{3+}:Mn^{4+} is calculated to be 36:100 in CMO and 24:100 in CNMO.

The schematic crystal structure of $Ca_3Mn_2O_7$ on the basis of the refined XRD parameters is presented in Fig. 1(b). Fig. 1(c) displays the schematic diagram of $Ca_3Mn_2O_7$ structure in the *ab* plane. It can be seen that the adjacent MnO_6 octahedrons are significantly rotated in the *ab* plane along the *c* axis and are tilted along the *b* axis, which result in off-centered apical oxygen ions. There are two possible sites for Ca ions, one is a 12-coordinate site (P site) in perovskite layers, and the other is a 9-coordinate site (R site) in the rock-salt block. The Na dopant in Ca-site preferentially occupies in the 12-coordinate site in perovskite layers.[8,13] Hence, dopant Na^+ ions would change the characteristics of MnO_6 octahedrons and Mn-O bond in the perovskite layer. The bond length and bond angle parameters obtained from Rietveld refinement of CMO and CNMO samples are shown in Table II, it is found that in CNMO all Mn–O bond length decrease and Mn–O_1–Mn bond angle slightly increases. This demonstrates that there is a Na dopant induced structural weakness of orthorhombic distortion. The orthorhombic distortion can be evaluated with a parameter δ with a definition equation $\delta = |b - c| / |b + c|$.[8] It is found that δ value is calculated to be 8.93×10^{-4} and 6.89×10^{-4} for CMO and CNMO, respectively, demonstrating a reduction of orthorhombic distortion induced by Na doping.

Raman spectroscopy is a powerful technique for detecting the subtle structural deformation in manganites. Fig. 2 presents the Raman scattering spectra with Lorentzian fittings of CMO and CNMO in the spectral range 50-1000 cm^{-1}. In CMO, indications of the typical peaks are well shown at 172, 208, 289, 464, 598 and 885 cm^{-1}. While in CNMO, these indications are well shown at 179, 212, 297, 468, 603 and 884 cm^{-1}. It can be observed that the peaks of CNMO have a shift toward high wave number in comparison with CMO, which can be attributed to the shortening of bond length.[14] In addition, it can be seen that the peaks at 598 (603) and 464 (468) cm^{-1} are the two characteristic sharp intensity peaks of CMO (CNMO). The former can be assigned to the in-plane symmetric stretching $B_{2g}(1)$ mode as indicated in the inset (a) of Fig. 2, and it originates from the vibrations of Mn^{3+}-O bonds in the MnO_6 octahedrons due to the presence of $1e_g$ electron in Mn^{3+}.[14–16] The later can be assigned to the out-of-plane stretching A_{1g} mode, as shown in the inset (b) of Fig. 2, which is originated from the vibrations of Mn^{4+}-O bonds in the MnO_6 octahedrons.[16,17] The intensity ratio

TABLE II. Bond length and bond angle parameters obtained from Rietveld refinement of CMO and CNMO samples.

Modes	Mn-O_1-Mn (deg)	Mn-O_1 (Å)	Mn-O_2 (Å)	Mn-O_3 (Å)	Mn-O_4 (Å)	$\sigma\times10^3$
CMO	163.192	1.9140	1.8735/1.8735	1.9089/1.8556	1.9069	22
CNMO	163.193	1.9128	1.8708/1.8727	1.9079/1.8548	1.9057	21

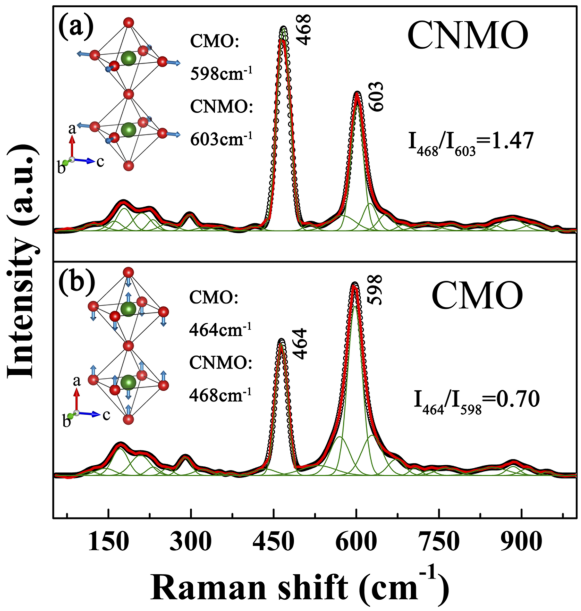

FIG. 2. Raman spectra of CMO and CNMO ceramics at room temperature. Inset (a) In-phase symmetric stretching $B_{2g}(1)$ mode. Inset (b) Out-of-phase stretching A_{1g} mode.

of the two strongest peaks increases from $I_{464}/I_{598} = 0.70$ to $I_{468}/I_{603} = 1.47$, which can be ascribed to the transformation of Mn^{3+} to Mn^{4+} (as confirmed by the XPS measurement shown in Fig. 4). Meanwhile, since Mn^{3+} ion is a Jahn-Teller (*JT*) ion,[18,19] the transformation of Mn^{3+} to Mn^{4+} would decrease the *JT* distortion. Hence, the Raman peak located at 603 cm^{-1} in CNMO is narrower than that at 598 cm^{-1} in CMO. In order to quantify the relative *JT* distortion of the MnO_6 octahedrons, the *JT* distortion parameter σ is employed, which is defined as $\sigma = \sqrt{\frac{1}{6}\sum_i (r_i - \langle r \rangle)^2}$, where r_i is a Mn-O bond length and $\langle r \rangle$ the average one.[8] As presented in Table II, the $\sigma \times 10^3$ value decreases from 22 to 21, indicating a reduction in the distortion of the MnO_6 octahedrons in CNMO. Such evolution trend of decreasing structural distortion induced by the Na doping is consistent with the XRD refinement results.

The morphology of both samples were analyzed by SEM, as shown in Fig. 3(a)–(b). CMO sample displays irregular shape, while CNMO sample displays approximate rod-like shape. The insets of Fig. 3(a)–(b) show the corresponding size distribution histogram. We can estimate that most of the particle size is in the range of 2-10 um for CMO, while 1.5-4 um for CNMO. This result clearly demonstrates that the average particle size is decreased with Na doping.

In order to further investigate the content variation of manganese element in samples, we performed XPS measurement on the Mn 2*p* region. Fig. 4 displays the XPS spectra analysis of the Mn 2*p* core-level regions with Lorentzian–Gaussian fitting for both samples, where core-level binding energies were aligned with respect to the C1*s* peak (284.6 eV). For CMO, the spectrum is split by the spin-orbit interactions into the Mn $2p_{3/2}$ and Mn $2p_{1/2}$ peaks, located at 641.7 and 653.3 eV, respectively. Moreover, the satellite to the Mn $2p_{1/2}$ peak is observed on the higher binding energy side (about 12 eV) of the main peak. In addition, the two peaks in the Mn $2p_{3/2}$ binding energy range with maxima at 641.3 and 642.3 eV correspond to Mn^{3+} and Mn^{4+} sates, respectively, and the tiny peak located at 644.5 eV corresponds to Mn^{4+} satellite.[20–22] Meanwhile, according to the fitting, the ratio of Mn^{3+}/Mn^{4+} is calculated to be 36:100 and 24:100 for CMO and CNMO, respectively, indicating that some of the Mn^{3+} gets oxidized to the Mn^{4+} state in CNMO sample.

There is no denying that the deviation of MnO_6 octahedrons based on Mn-O bond length and Mn–O_1–Mn bond angle would have an important impact on the magnetic characteristics of the sample. Fig. 5(a)–(b) display the magnetizations of CMO and CNMO as a function of temperature at zero field cooling (ZFC) and field cooling (FC) modes under a magnetic field of 100 Oe at 5 K.

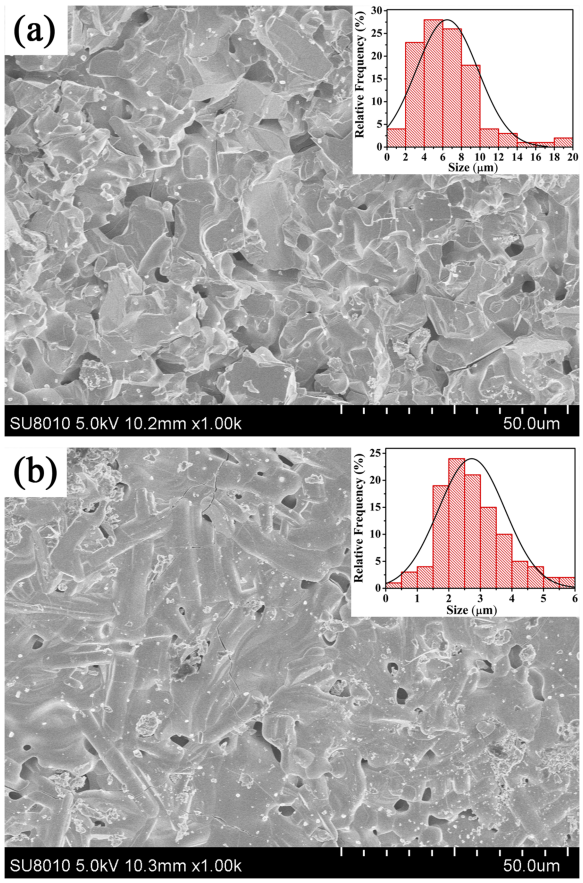

FIG. 3. (a)-(b) SEM images for CMO and CNMO samples, respectively. The insets of (a)-(b) are the corresponding statistic particle size distribution.

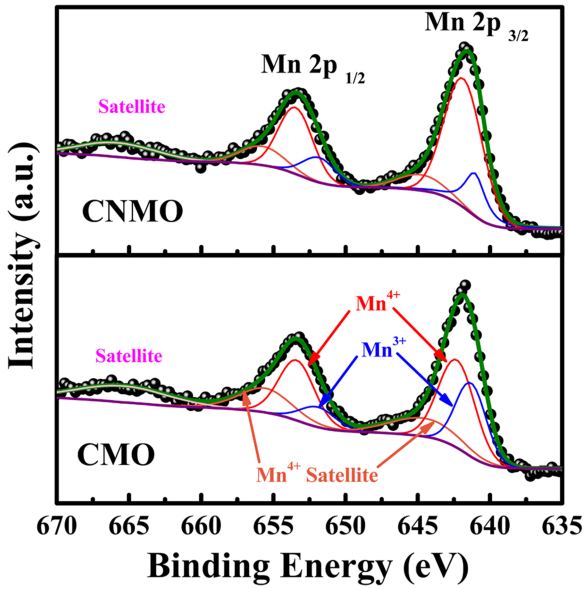

FIG. 4. The X-ray photoelectron spectroscopic (XPS) spectra of Mn 2*p* for CMO and CNMO ceramics at room temperature.

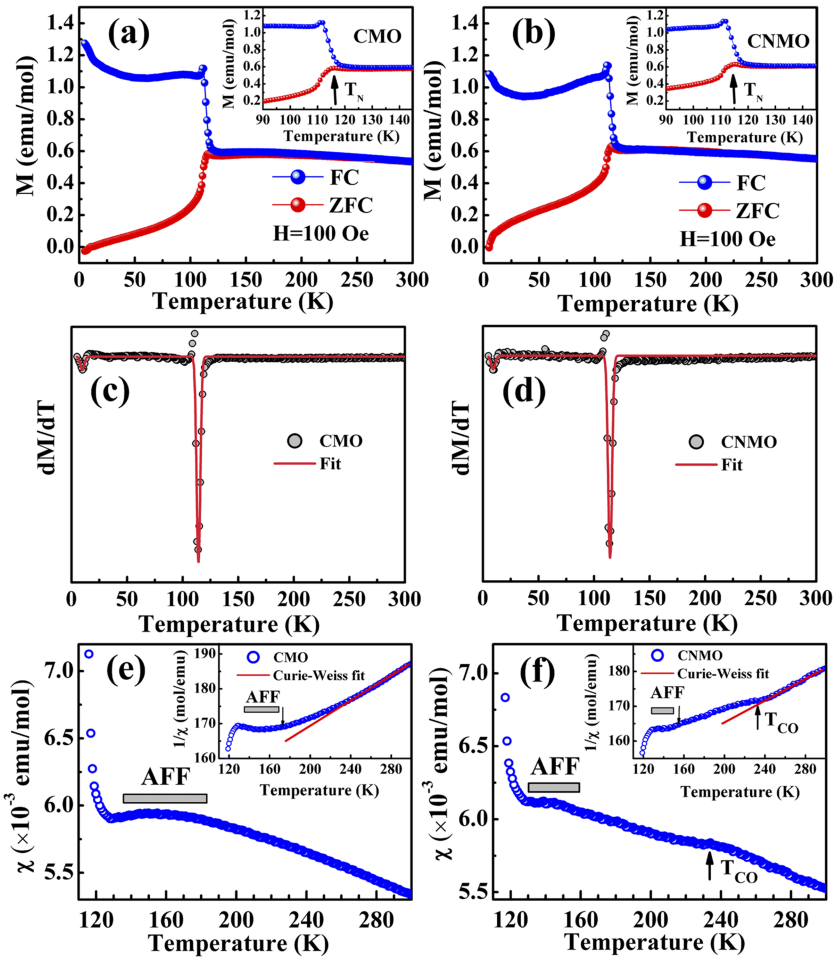

FIG. 5. (a) and (b) Temperature dependences of the ZFC and FC magnetizations of CMO and CNMO ceramics at $T = 5$ K under a magnetic field of 100 Oe. (c) and (d) Derivatives of the Magnetization (dM/dT) and the fitted Lorentzian–Gaussian function curves (pink line) of both samples. (e) and (f) Temperature dependence of the susceptibility of both samples. Rectangular shadow indicates the short-range antiferromagnetic fluctuations (AFF's). Insets are the inverse susceptibility curves (blue circles) with Curie–Weiss fits (red solid lines).

It can be seen that the ZFC and FC magnetization branches demonstrate a noticeable bifurcation below 120 K and shows strong overlapping above 120 K for both samples. In addition, small broaden cusps are observed in the region between 110 and 120 K of ZFC curves in the inset of Fig. 5(a)–(b), which are identified with T_N of CMO and CNMO. In order to determine T_N of both samples, the temperature dependence of the dM/dT with Lorentzian–Gaussian fitting is plotted in Fig. 5(c)–(c). The Néel temperature, defined as the temperature corresponding to the minimum of dM/dT, is about 111 K for both samples within the range of error. The ZFC and FC magnetization branches demonstrate a noticeable bifurcation below 120 K, which indicates the possibility of existence of FM components. This can be ascribed to the inhomogeneous magnetic state, because the small amount of Mn^{3+} in the Mn^{4+} matrix can lead to the formation of local FM clusters embedded in the AFM matrix.[23–25]

Fig. 5(e)–(f) show the temperature dependence of the susceptibility of both samples. As the insets shown, at the high temperature, the experimental data over the interval for both samples were fitted according to the Curie-Weiss (CW) law, $1/\chi = (T - \theta_{CW})/C$, where χ is the susceptibility, C the Curie-Weiss constant, T the temperature, and θ_{CW} the Curie-Weiss temperature. The θ_{CW} values obtained from CW fits are: θ_{CW} = -756 K for CMO and θ_{CW} = -843 K for CNMO. The negative sign and the high absolute value of θ_{CW} for both samples demonstrate the existence of strong AFM exchange interactions between the manganese ions.[26] Moreover, compared with CMO, the larger

absolute value of θ_{CW} in CNMO indicates an enhancement of antiferromagnetism.[25,26] However, the θ_{CW} value is roughly sevenfold too high to agree with the T_N, which maybe produced by the substantial covalency and AFM interactions.[27,28] It is noted that at a temperature of approximately 235 K [see Fig. 5(f)], denoted by T_{CO}, a subtle $\chi(T)$ shoulder is observed, which is identified with the charge- and orbital- (CO) ordering temperatures.[28–30] And the shoulder would consistent with its weaker FM correlation.[28] When we turn to the 130-175 K temperature regions in the $\chi(T)$ curves, an onset change will be found in both samples. M. V. Lobanov et al. found that the effective magnetic dimensionality D of $Ca_3Mn_2O_7$ is between 2 and 3 (i.e. quasi-2D).[8] In such quasi-2D material, a broad maximum is always visible above T_N, which is caused by the slowly weakened antiferromagnetic fluctuations (AFF's).[28] When the effect is presented in the inverse susceptibility [$\chi^{-1}(T)$], these AFF's are reflected by an upturn from CW behavior.[8,28] As the inset shown, the extended range of deviation from CW-like behavior reflects this feature.

The field-dependent magnetization hysteresis (M-H) loops of the samples at 5 K are presented in Fig. 6. For both samples, M increase almost linearly with H, indicating the dominant interactions are AFM.[25] The AFM phase can be ascribed to the coupling between Mn^{4+} matrix ions through a super-exchange interaction via the O^{2-} ion in octahedral sites.[31] Moreover, for both samples, a small hysteresis is observed in the M-H curves, which indicates the existence of weak ferromagnetic (WFM) component in the samples. The observed WFM component can be attributed to the double-exchange interaction between Mn^{4+} and Mn^{3+} ions.[32] The inset (a) of Fig. 6 shows the enlargement of M-H curves of the magnetic field range of -0.45 kOe to +0.23 kOe. It can be observed that the hysteresis loops are significantly shifted towards negative magnetic field, which is expected for the *EB* effect. The *EB* and coercive fields (H_{EB}, H_C) are defined as $H_{EB} = -(H_1 + H_2)/2$ and $H_C = (H_2 - H_1)/2$, respectively, where H_1 and H_2 are the negative and positive fields at $M = 0$.[33] The H_{EB} value increases from 78 Oe in CMO to 120 Oe in CNMO and the H_C value increases from 142 Oe in CMO to 210 Oe in CNMO.

To ascertain the presence of *EB* in CNMO, we studied the training effect. Variation of the fields $-H_1$ and H_2 with the number of recurrent hysteresis loops n at 5 K are shown in the inset (b) of Fig. 6. Both the magnitudes of $-H_1$ and H_2 decrease with increasing n. The field H_{EB} is found to diminish by ~45% after the first magnetization reversal, and then relax slowly with training by seven recurrent magnetization cycles, as shown in the inset (c) of Fig. 6. This can be attributed to the AFM

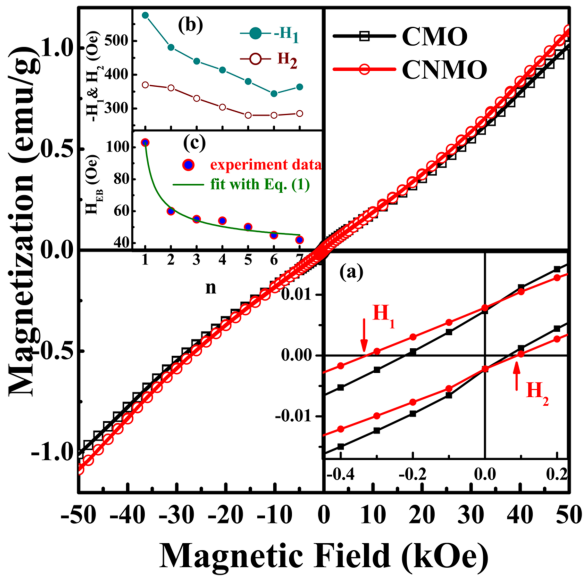

FIG. 6. Field-dependent magnetization hysteresis (M-H) loops of CMO and CNMO ceramics at 5 K. Inset (a) The enlargement of M-H loops at magnetic field range from -0.45 kOe to +0.23 kOe. H_1 and H_2 are the negative and positive fields at $M = 0$. Inset (b) and (c) Variations of $-H_1$ & H_2 and H_{EB} with the number of recurrent hysteresis loops n at 5 K, respectively.

domain rearrangement at the interface, due to the existence of inhomogeneous magnetic state in the sample.[34,35]

The *EB* training effect can be described within the frame of Spin-Configuration-Relaxation (SCR) model, with a general recursive formula as follows:

$$H_{EB}(n) = H_{EB}(n \to \infty) + A_f \exp\left(-n/P_f\right) + A_i \exp(-n/P_i), \quad (1)$$

where A_f and P_f are parameters related to the changes in the frozen spins, A_i and P_i evolving parameters linked to the rotatable spin component at the FM/AFM interface.[33,35] Here, the parameter A have dimension of magnetic field, while parameter P is an indicative of relaxation rate of the process. The olive solid line in the inset (c) of Fig. 6 is the best fit of equation (1) to the $H_{EB}(n)$ data. The obtained fitting parameters are: $H_{EB}(n \to \infty) = 40.15\ Oe$, $A_f = 1891.16\ Oe$, $P_f = 0.26$, $A_i = 31.69\ Oe$ and $P_i = 3.95$. It is apparent that a contribution from the frozen uncompensated AFM spins at the interface is huge at the initial stage of training, while the rotatable AFM component is much weaker and relaxes about 15 times slower as compared to the first one. In brief, the existence of the distinctive training effect provides evidence for the true *EB* effect in CNMO.

Intuitively, the increase of *EB* field in CNMO can be explained within a model of size-variable nanoscale ferromagnetic clusters embedded in an antiferromagnetic matrix. In accordance with the classic Meiklejohn-Bean (MB) model, the *EB* is from the interfacial exchange coupling between FM phase and AFM phase in compounds with small enough volume of the FM phase.[36,37] A simple MB model can be written as:

$$H_{EB} = \left(-\frac{6J}{M_{FM}D}\right) \times \sqrt{1 - \left(\frac{J}{2K_{AFM}t_{AFM}}\right)^2}, \quad (2)$$

where J is the interfacial exchange energy, M_{FM} the magnetization of the FM layers, D the FM clusters size, K_{AFM} the AFM anisotropy, t_{AFM} the thickness of the AFM matrix.[33,38–41] For small FM particles, the H_C is effectively controlled by the particle size D, as $H_C = a + b/D$, where a and b are constants.[41,42] Thus, compared with CMO, the increased H_C indicates a smaller D value of FM cluster in CNMO sample. Moreover, the decreased D leads to a better dispersion of FM clusters in CNMO sample, which could increase the thickness t_{AFM} and anisotropy energy $K_{AFM}t_{AFM}$ of the AFM layers.[39] Thus, on the basis of equation (2), the increase of *EB* field in CNMO can be explained with the decreased D value and increased $K_{AFM}t_{AFM}$.

CONCLUSIONS

In summary, CMO and CNMO ceramics were synthesized by standard solid-state reaction method. We have studied the structural and magnetic properties of both samples. It is found that Na doping effectively weakens the structural distortion as decreasing the orthorhombic distortion and the *JT* distortion. Both samples undergo an AFM transition around 111 K. Moreover, with Na substitution, an increased *EB* field is found in CNMO, which may be explained within the MB model.

SUPPLEMENTARY MATERIAL

See supplementary material for the synthetic route and characterization method of CMO and CNMO ceramics, as well as the lattice structure parameters obtained from Rietveld refinement and XPS spectra analysis of Mn_{2p}.

ACKNOWLEDGMENTS

This work was funded by the National Natural Science Foundation of China (project no. 51572193 and 11104202), and the Natural Science Foundation of Tianjin (No. 17JCYBJC17600).

[1] N. A. Benedek and C. J. Fennie, Phys. Rev. Lett. **106**, 107204 (2011).
[2] A. T. Mulder, N. A. Benedek, J. M. Rondinelli, and C. J. Fennie, Adv. Funct. Mater. **23**, 4810 (2013).
[3] Y. S. Oh, X. Luo, F. T. Huang, Y. Z. Wang, and S. W. Cheong, Nature Materials **14**, 407 (2015).
[4] A. B. Harris, Phys. Rev. B **84**, 064116 (2011).
[5] W. Zhang and P. Q. Tong, Chin. Phys. B **22**, 066201 (2013).

[6] W. K. Zhu, L. Pi, Y. J. Huang, S. Tan, and Y. H. Zhang, Appl. Phys. Lett. **101**, 192407 (2012).
[7] M. V. Lobanov, M. Greenblatt, E. N. Caspi, J. D. Jorgensen, D. V. Sheptyakov, B. H. Toby, C. E. Botez, and P. W. Stephens, J. Phys.: Condens. Matter **16**, 5339 (2004).
[8] M. V. Lobanov, S. Li, and M. Greenblatt, Chem. Mater. **15**, 1302 (2003).
[9] T. Toyoda, N. Sasaki, K. Shimada, M. Okube, and S. Sasaki, Jpn. J. Appl. Phys. **50**, 041101 (2011).
[10] T. Yamashita, K. Kubo, K. Nakao, T. Sakurai, S. Ikegawa, J. Sugiyama, and H. Yamauchi, Phys. Rev. B **53**, 14470 (1996).
[11] H. Zhang, W. F. Liu, P. Wu, X. Hai, M. C. Guo, X. J. Xi, J. Gao, X. Wang, F. Guo, X. L. Xu, C. Wang, G. Y. Liu, W. G. Chu, and S. Y. Wang, Nanoscale **6**, 10831 (2014).
[12] R. D. Shannon, Acta Cryst. A **32**, 751 (1976).
[13] M. A. Green and D. A. Neumann, Chem. Mater. **12**, 90 (2000).
[14] M. N. Iliev, M. V. Abrashev, J. Laverdière, S. Jandl, M. M. Gospodinov, Y. Q. Wang, and Y. Y. Sun, Phys. Rev. B **73**, 064302 (2006).
[15] S. Elsässer, J. Geurts, A. A. Mukhin, and A. M. Balbashov, Phys. Rev. B **93**, 054301 (2016).
[16] B. Singh, Mater. Lett. **156**, 76 (2015).
[17] K. Yamamoto, T. Kimura, T. Ishikawa, T. Katsufuji, and Y. Tokura, Phys. Rev. B **61**, 14706 (2000).
[18] D. C. Chen, D. Ding, X. X. Li, G. H. Waller, X. H. Xiong, M. A. El-Sayed, and M. L. Liu, Chem. Mater. **27**, 6608 (2015).
[19] M. Inaba, Y. Iriyama, Z. Ogumi, Y. Todzuka, and A. Tasaka, J. Raman Spectrosc. **28**, 613 (1997).
[20] S. P. Wu, Y. C. Lv, M. J. Lu, and Z. Q. Lin, J. Mater. Chem. C **3**, 3121 (2015).
[21] Y. Q. Guo, Y. Tong, P. Z. Chen, K. Xu, J. Y. Zhao, Y. Lin, W. S. Chu, Z. M. Peng, C. Z. Wu, and Y. Xie, Adv. Mater. **27**, 5989 (2015).
[22] Y. K. Hsu, Y. C. Chen, Y. G. Lin, L. C. Chen, and K. H. Chen, J. Mater. Chem. **22**, 2733 (2012).
[23] X. H. Huang, Z. L. Jiang, X. F. Sun, and X. G. Li, J. Am. Ceram. Soc. **94**, 1324 (2011).
[24] V. B. Shenoy, T. Gupta, H. R. Krishnamurthy, and T. V. Ramakrishnan, Phys. Rev. B **80**, 125121 (2009).
[25] X. K. Zhang, S. L. Tang, and Y. W. Du, J. Phys. Chem. C **115**, 2644 (2011).
[26] W. J. Lu, Y. P. Sun, R. Ang, X. B. Zhu, and W. H. Song, Phys. Rev. B **75**, 014414 (2007).
[27] D. Fawcett, J. E. Sunstrom, M. Greenblatt, M. Croft, and K. V. Ramanujachary, Chem. Mater. **10**, 3643 (1998).
[28] D. Fawcett, E. Kim, and M. Greenblatt, Phys. Rev. B **62**, 6485 (2000).
[29] M. T. Fernández-Díaz, J. L. Martínez, J. M. Alonso, and E. Herrero, Phys. Rev. B **59**, 1277 (1999).
[30] Y. Murakami, D. Shindo, H. Chiba, M. Kikuchi, and Y. Syono, Phys. Rev. B **55**, 15 043 (1997).
[31] J. Kanamori, J. Phys. Chem. Solids. **10**, 87 (1959).
[32] P. Chai, X. J. Liu, M. F. Lu, Z. L. Wang, and J. Meng, Chem. Mater. **20**, 1988 (2008).
[33] R. Puzniak, V. Markovich, A. Wisniewski, P. Iwanowski, S. Kolesnik, and B. Dabrowski, Ceram. Int. **42**, 8453 (2016).
[34] Y. Q. Zhang, W. B. Rui, Z. Shi, S. M. Zhou, M. Yang, B. You, and J. Du, J. Supercond. Nov. Magn. **29**, 531 (2016).
[35] S. K. Mishra, F. Radu, H. A. Dürr, and W. Eberhardt, Phys. Rev. Lett. **102**, 177208 (2009).
[36] W. H. Meiklejohn and C. P. Bean, Phys. Rev. **105**, 904 (1957).
[37] W. H. Meiklejohn, J. Appl. Phys. **33**, 1328 (1962).
[38] F. Radu and H. Zabel, Springer Tracts in Modern Physics **227**, 97 (2008).
[39] M. S. Lund, W. A. A. Macedo, K. Liu, J. Nogués, I. K. Schuller, and C. Leighton, Phys. Rev. B **66**, 054422 (2002).
[40] J. Nogués, J. Sort, V. Langlais, V. Skumryev, S. Suriñach, J. S. Muñoz, and M. D. Baró, Phys. Rep. **422**, 65 (2005).
[41] I. Fita, V. Markovich, A. Wisniewski, R. Puzniak, C. Martin, V. N. Varyukhin, and G. Gorodetsky, Phys. Rev. B **88**, 064424 (2013).
[42] B. D. Cullity, *Introduction to Magnetic Materials* (Addison-Wesley, Reading, MA, 1972).